Improving Efficiency and Stability of Perovskite Solar Cells Enabled by A Near-Infrared-Absorbing Moisture Barrier

Qin Hu[1,2†], Wei Chen[3,6†], Wenqiang Yang[4†], Yu Li[2,5], Yecheng Zhou[7], Bryon W. Larson,[8] Justin C. Johnson,[8] Yi-Hsien Lu[2], Wenkai Zhong[9], Jinqiu Xu[5], Liana Klivansky[10], Cheng Wang[9], Miquel Salmeron[2], Aleksandra B. Djurišić[3], Feng Liu[5]*, Zhubing He[6]*, Rui Zhu[4,11]* and Thomas P. Russell[1,2]*

[1]Department of Polymer Science and Engineering, University of Massachusetts, Amherst, Massachusetts 01003, USA.
[2]Materials Sciences Division, Lawrence Berkeley National Laboratory, Berkeley, California 94720, USA.
[3]Department of Physics, The University of Hong Kong, Pokfulam, Hong Kong SAR.
[4]State Key Laboratory for Artificial Microstructure and Mesoscopic Physics, School of Physics, Frontiers Science Center for Nano-optoelectronics & Collaborative Innovation Center of Quantum Matter, Peking University, Beijing, China.
[5]Frontiers Science Center for Transformative Molecules, School of Chemistry and Chemical Engineering, Shanghai Jiao Tong University, Shanghai 200240, P. R. China.
[6]Department of Electrical and Electronic Engineering, Shenzhen Key Laboratory of Full Spectral Solar Electricity Generation (FSSEG), Southern University of Science and Technology, No. 1088, Xueyuan Rd., Shenzhen, 518055, Guangdong, P.R. China.
[7]School of Materials Science & Engineering, Sun Yat-sen University, Guangzhou 510275 Guangdong, P. R. China.
[8]National Renewable Energy Laboratory, Golden, Colorado, 80401, USA.
[9]Adavanced Light Sources, Lawrence Berkeley National Laboratory, Berkeley, California 94720, USA.
[10]Molecular Foundry, Lawrence Berkeley National Laboratory, Berkeley, California 94720, USA.
[11]Collaborative Innovation Center of Extreme Optics, Shanxi University, Taiyuan, Shanxi, China.

† These authors contributed equally to this work.
*Corresponding Authors: fengliu82@sjtu.edu.cn (F. L.), hezb@sustech.edu.cn (Z.H.), iamzhurui@pku.edu.cn (R. Z.), and tom.p.russell@gmail.com (T. P. R.)

Keywords: NIR Absorption; Moisture Barrier; Molecular Bonding; Perovskite Solar Cells; Charge Carrier Dynamics; Device Stability

Summary

A new strategy to introduce a multi-functional interface layer (MFIL) that performs multiple functions: 1) electron transport, 2) moisture barrier, 3) near-infrared photocurrent enhancement, 4)

trap passivation and 5) ion migration suppression, to simultaneously improve the device efficiency and long-term stability of perovskite solar cells (PSCs) is demonstrated. After a series of material screening, a new dithienothiophen[3,2-b]-pyrrolobenzothiadiazole derivative, Y6, was chosen to replace the most commonly used electron transport layer, PCBM, in the inverted structured heterojunction PSCs. A significantly improved power conversion efficiency of 21.0% under AM 1.5G 100 $mW \cdot cm^{-2}$ solar irradiation was achieved along with the remarkable stability (up to 1700 hours) under various external stimuli (light/heat/moisture), which is among the top performances for inverted PSCs. Notably, for the operational stability of non-encapsulated PSCs under maximum power point (MPP) tracking with AM1.5G simulated light illumination and humidity of 60%-65%, the Y6-based device maintained over 95% of its initial efficiency (T_{95} lifetime) after 1300 min, which is 20 times longer than the PCBM-based device. In addition, the crystallization and aggregation of Y6 were precisely optimized with different solvent environments, and a deep understanding of the perovskite/MFIL interface at a molecular level was presented by the advanced synchrotron-based X-ray characterizations. Charge carrier dynamics were further explored by steady-state microwave conductivity and ultrafast transient absorption spectroscopy. Correlations between molecular orientation, interface molecular bonding, trap state density, non-radiation recombination, and device performance were established. These results offer new insights on designing advanced interlayers, simplifying the device structure in PSCs, and enhancing device efficiency and stability, all of which will accelerate the market readiness of perovskite-based optoelectronics.

Introduction

Organic-inorganic hybrid perovskite thin film solar cells have emerged as an efficient solar-energy technology with excellent power conversion efficiencies (PCEs), ease of fabrication, and low production cost, proving to be a game changer in photovoltaics.[1-3] Significant effort has been devoted to optimize device efficiencies[4] and to further understand inherent material properties.[5] Some strategies, including crystallization and morphology optimization of perovskite thin films,[6] composition-tunable alloying[7] for increasing light absorption, and interface engineering[8] within the device structure, have been adapted to enhance the PCEs. Despite these efforts to improve device performance, the lifespan of perovskite solar cells (PSCs) is still too short for practical use.[9,10] Thus, simultaneously improving device efficiency and stability has become the most important issue at present. The inherent "soft" crystal lattice of perovskite solids is one of the key reasons for poor stability, which makes PSCs vulnerable to aging stresses such as UV-light, moisture, electric fields and thermal annealing. In addition, structural defects in the bulk and on the surfaces of perovskite polycrystalline thin films, ion migration, hygroscopic additives and the thermal instability of charge transporting layers, are also contributors to PSCs' performance deterioration.[11] Various approaches have been applied to improve the perovskite quality and critical interfaces, and PSCs can now survive under environment stresses from hours to months. For instance, to selectively oxidize Pb^0 and reduce I^0 defects, Europium ion pairs Eu^{3+}-Eu^{2+}, can be added as the "redox shuttle", increasing device efficiency and longevity.[9] Ionic liquid additives[12] have also been shown to improve the surface energetic alignment and suppress ion migration, resulting in longer-lasting output. Moreover, a double layer perovskite structure with *in-situ* reaction of hydrophobic chemicals (n-hexyl trimethyl ammonium bromide[13] or lead

sulfate[14]) can passivate the perovskite surface, yielding higher open-circuit voltages (V_{oc}) and enhanced moisture resistance.

In addition to the optimization of the perovskite active layer, significant contributions have also been made to reduce surface disorder, improve charge extraction, and enhance the chemical stability of the electron/hole transporting layer (ETL/HTL) towards the goal of maximizing device stability. Compared to the regular n-i-p structure, the p-i-n (aka inverted) structure shows great potential to realize long-term operational stability, due to the use of stable metal oxide semiconductors or undoped conjugated polymers/small molecules as the interface layers.[15-17] Having a robust ETL in p-i-n PSCs is also needed for implementing a perovskite as the front cell in perovskite:silicon or all-perovskite tandem solar cells.[18,19] Furthermore, inverted PSCs are also compatible with plastic substrates which require low-temperature fabrication for flexible devices.[20] Unfortunately, p-i-n PSCs have not kept pace with n-i-p PSCs in device efficiencies due to lower short current densities (J_{sc})[21] and/or larger open circuit voltage (V_{oc}) losses induced by non-radiative recombination.[22] On top of poorer performance, inverted PSCs also usually exhibit modest stability against water and light, mainly due to the use of fullerenes with low crystallinity and large aggregation as the ETL.[23] Therefore, new strategies to realize both high efficiencies and high stabilities for inverted PSCs are urgently needed.

Here, we introduce a multi-functional interface layer (MFIL) approach to combine the roles of 1) electron transport, 2) moisture barrier, 3) near-infrared photocurrent enhancement, 4) trap passivation, and 5) ion migration suppression in inverted PSCs, and to simultaneously improve the device efficiency and long-term stability of perovskite solar cells. Compared to the fullerenes, the non-fullerenes can be easily chemically tuned to obtain superior physical properties, such as light absorption, energy level and charge generation.[24-27] Thus, non-fullerenes have the great potential

to realize these functions of MFILs. A new small-bandgap non-fullerene acceptor (NFA), Y6 (as shown in Figure 1), a popular BT-core-based fused-unit dithienothiophen[3,2-b]-pyrrolobenzothiadiazole (TPBT) derivative, was screened from a series of narrow-band gap acceptor materials to replace the commonly used PCBM without any additive or donor materials in the solid thin film. The molecular orientation, the electronic states of local structures, and the surface morphology of the Y6 layer were systematically investigated for the full device stack. The high mobility and suitable energy levels of Y6 matched the perovskite active layer quite well,[24] and the narrow optical-bandgap extended the photoresponse cutoff from ~765 nm to ~940 nm, resulting in an improved integrated J_{sc}. Interfacial bonding interactions between the perovskite and Y6 were further analyzed using advanced surface spectroscopies: X-ray photoelectron spectroscopy (XPS) and synchrotron-based X-ray total fluorescence yield (TFY). We find that chemical complexing of electron-rich C-S-C, C=O, C≡N and C-F functional groups in Y6 with the empty orbitals in Pb^{2+} or other electron traps at the perovskite interface led to reductions in trap state density and non-radiative recombination, enhanced electron extraction, and suppressed ion migration in operation, resulting in the enhanced V_{oc}, fill factor (FF) and a champion PCE of 21.0%. We also used steady-state and time-resolved photoluminescence (TRPL) spectra, steady-state microwave conductivity (SSMC) measurements and ultrafast transient absorption spectroscopy (TAS) to elucidate the underlying charge carrier dynamics. Furthermore, in combination with the hydrophobic properties of Y6, which impedes water penetration, the surface chemical stability, intrinsic photo-stability at standard AM1.5G conditions, ambient stability with humidity of 60%-65%, and thermal stability at 85 °C were all increased significantly for Y6-based devices in contrast to PCBM-based devices. This MFIL strategy opens up new pathways for ETL design and optimization for inverted PSCs, since it concomitantly enhances both device efficiency

and stability, thus more broadly accelerating the market readiness of perovskite-based optoelectronics.

Results and Discussion

MFIL Screening and Molecular Orientation

Figure 1a shows the device architecture of the inverted planar heterojunction perovskite solar cells studied in this work. A cross-sectional scanning transmission electron microscopy (STEM) image is shown in Figure S1. Poly(triarylamine) (PTAA) is used as hole transport layer (HTL), and the tri-cation CsFAMA perovskite with bandgap of ~1.6 eV was fabricated as photoactive layer (see details in the Supporting Information). We observed a uniform, compact morphology of the perovskite layer from the SEM image (Figure S1b). As a control, PCBM was used as the electron transport layer (ETL) to contrast a series of narrow-band gap non-fullerene acceptors (NFAs)[24-28] (Y6, IEICO-4F and IOIC-2Cl). The UV-vis absorption spectra of tri-cation CsFAMA perovskite and the ETLs are shown in Figure 1b. All of the NFAs studied here extend the light-absorption from the visible (~765 nm) to the near-infrared (NIR) region (~950 nm). However, when we fabricated full devices to screen these ETLs, only the Y6-based device gave a higher efficiency (20.5%, Figure 1d) than the PCBM control, a result of a V_{oc} of 1.11 V, FF of 0.78 and J_{sc} of 23.7 mA·cm^{-2} with contribution from the extended NIR photoresponse as shown in the EQE spectrum (Figure 1e). In contrast, the IOIC-2Cl and IEICO-4F devices both decreased the relative device performance with PCEs of 13.6% (V_{oc} = 1.03 V, FF = 0.54, J_{sc} = 24.5 mA·cm^{-2}) and 10.8% (V_{oc} = 1.04 V, FF = 0.46, J_{sc} = 22.5 mA·cm^{-2}), respectively. The very poor FF and V_{oc} results were likely caused by mismatched energy level alignments and high interfacial charge recombination as shown in Figure 1c. Thus, we propose the first guidelines to screen effective narrow-bandgap NFAs to as candidates for a multi-functional interfacial layer (MFIL): i) complementary light

harvesting, ii) a favorable surface energetic alignment (deeper LUMO/HOMO energy than perovskite), iii) suitable charge mobility and iv) electron donating functional groups to passivate the perovskite surface. Of the three NFAs here, Y6 is the only one that meets the criteria set for MFILs, though we also expect that inorganic semiconductor materials, such as NIR-absorbing quantum dots, could do so as well, as long as the energetic and functional group requirements are also fulfilled.

In organic semiconductors, exciton dissociation and charge transport are sensitive to molecular order. We found that the crystallization and aggregation of Y6 can be precisely controlled in different solvent environments. The π-π stacking of Y6 films for efficient charge extraction was investigated by grazing incident X-ray diffraction (GIXD), as shown in Figure 2a. Three typical solvents with different boiling points, chloroform (CF), toluene (Tol) and chlorobenzene (CB), were used to process the Y6 films. The CF-processed Y6 (Y6-CF) film has a dominant π-π stacking diffraction peak at q ~ 1.77 $Å^{-1}$ in the out-of-plane (OOP) direction with a d-spacing of 3.55 Å and a crystalline coherence length (CCL) of 21.36 Å (calculated by Scherrer equation[29] and the half of the maximum intensity was calculated from Gaussian fitting), forming a typical face-on orientation. The (110) peak and (11-1) peaks, simulated from single crystal structure with the unique 2D packing with polymer-like conjugated backbone (as shown in Figure S2), in the in-plane (IP) direction are located at q ~ 0.29 $Å^{-1}$ and q ~ 0.42 $Å^{-1}$ with d-spacing of 21.65 Å and 14.95 Å, respectively. The GIXD scattering results and the related single crystal simulation indicate that the banana-like Y6 molecules grow or stack normal to substrate interface resulting in more efficient charge transfer by π-π stacking.[30] The diffraction profiles from the toluene-processed Y6 (Y6-Tol) and CB-processed Y6 (Y6-CB) films are quite similar, but the π-π stacking reflection is much weaker and less oriented in comparison to Y6-CF, suggesting reduced

crystallinity and a more random orientation. The enhanced scattering at q ~ 1.20 $Å^{-1}$ indicates an increased amorphous content in Y6-CB and Y6-Tol. The corresponding integrated profiles in the IP and OOP directions are shown in Figure 2b. The detailed CCL and areas of the characteristic peaks are summarized in Figure 2d (OOP) and Figure S3 (IP). The Y6-CF has a greater peak area and CCL for the π-π stacking and (11-1) reflections, in comparison to Y6-CB and Y6-Tol, while they have close d-spacings. In addition, the peak areas of π-π stacking reflections in OOP and IP are summarized in Figure 2e. The peak area ratio of the π-π stacking reflection in OOP to that in IP for Y6-CF is ~3.5, while the Y6-CB and Y6-Tol values are close to 1.0, indicating that the π-π stacking for the Y6-CF film is significantly more oriented normal to the substrate, reducing the surface disorder at the perovskite/Y6 interface and enhancing efficient electron extraction and transport from the perovskite active layers, as shown in Figure 2c.

The morphology and electronic properties of the surface of Y6 films were further investigated by Kelvin probe force microscope (KPFM). Figure S4 shows the surface topography of the perovskite/Y6 films. The root mean square (rms) roughness values are 5.49 nm (Y6-CF), 5.95 nm (Y6-Tol) and 8.28 nm (Y6-CB), which could correspond to effects of different solvent vapor pressures during the film drying process. The solvent-rich films (with high-boiling point solvent) have insufficient time to heal surface roughness caused by Marangoni instabilities, reducing the film roughness.[31] The redshift of the longest-wavelength light absorption peak (~840 nm) in the UV-vis spectra, as seen in Figure S5, suggest the enhanced molecular packing with larger aggregations in Y6-Tol and Y6-CB films, this is consistent with the recent report in Y6 based organic solar cells.[30] The contact potential difference (CPD) images of perovskite/Y6 films are shown in Figure 2f. In agreement with the surface topography, the variation of CPD value for Y6-CF is 0.016 V, Y6-Tol is 0.022 V whereas Y6-CB is 0.024 V. The similarity of the CPD values

suggests that different molecular packing or surface morphology in Y6 films has little influence on the surface potential. In summary, compared to Y6-CB and Y6-Tol, the Y6-CF film shows the dominant face-on orientation with the highest degree of crystallinity (GIXD results), as well as the smoothest surface topography and surface potential distribution (KPFM). Therefore, the best device performance with Y6-CF was expected.

Device performance and Interface Characterizations

Inverted PSC devices incorporating Y6 layers with different molecular orientations (based on casting solvent) were fabricated and characterized. The device parameters measured under a standard AM 1.5G solar illumination (100 $mW \cdot cm^{-2}$) are summarized in Table S1. All the Y6-based devices have very similar J_{sc} and V_{oc}. However, the Y6-CF device had the highest fill factor (FF) of 0.78 and the highest PCE of 20.5%, while the Y6-Tol and Y6-CB had lower FF of 0.70 and 0.68, resulting in PCEs of 17.9% and 17.7%, respectively. A sharp decrease in the FFs of Y6-Tol and Y6-CB based devices is ascribed to the increased series resistance (Rs) and decreased shunt resistance (Rsh) (shown in Table S1), which could be caused by increased surface roughness and less efficient interfacial charge transport. These results further argue that the face-on orientation and π-π stacking in the Y6-CF film is responsible for more efficient extraction and transport of electrons from the perovskite layer. Moreover, the device performance also confirms that the photoexcited excitons from Y6-CF layer can be dissociated at the interface and contributes to a higher J_{sc}. This is further evidenced by the enhanced external quantum efficiency (EQE) in the NIR region of Y6-CF devices (Figure S6). The Y6-CF devices were also optimized by varying the film thickness using different solution concentrations (Figure S7); a 9.5 mg/ml solution giving a thickness of 46.3 nm (Table S2) yielded the best performance. When a very thin layer of C_{60} (20

nm) was added on the Y6-CF film to further enhance the charge extraction,[32] both the FF and V_{oc} increased, yielding a PCE approaching 21%. As a result, this approach was used for all devices.

The device performance with Y6 and traditional PCBM was further examined. Compared to the PCBM-based device, the V_{oc} (from 1.10 V to 1.12 V) and FF (from 0.77 to 0.79) of the Y6-based device are slightly enhanced while the J_{sc} increased significantly from 22.64 mA·cm^{-2} to 23.68 mA·cm^{-2}, leading to the enhancement in the PCE from 19.2% to 21.0%, as shown in Figure 3a. The EQE spectrum of the Y6 device (Figure 3b) showed an extended photoreponse in the NIR region (~940 nm), demonstrating the synergistic functions of Y6, both as a photoactive layer and a charge transport medium. The integrated current densities from the EQEs are 21.86 mA·cm^{-2} (PCBM) and 22.85 mA·cm^{-2} (Y6), which are consistent with the enhanced J_{sc} from the *J-V* curves. It should be noted that the devices have negligible hysteresis under a range of different scanning conditions. In addition, the stabilized power output (SPO) at maximum power point (MPP) were also tracked to confirm the efficiency reliability. As shown in Figure S8, the Y6-based devices had a stabilized efficiency of 20.9%, while the PCBM-based device had an output of 19.1%. In addition, the Y6-based devices also showed excellent reproducibility with small standard deviations, as shown in Table S3 based on 20 devices.

To explore the origins for the enhanced device performance of Y6-based devices, the carrier transport properties were determined. Both steady-state and time-resolved photoluminescence (TRPL) spectra were measured (Figure 3c and Figure 3d). The PL peaks of perovskite (PVSK)/Y6 and PVSK/PCBM films are both located at ~767 nm. Compared to the pure perovskite sample, the PL intensities of both the PVSK/PCBM and PVSK/Y6 sample decreased markedly, indicating a comparable charge extraction for Y6 in comparison to PCBM. The charge recombination kinetics were measured by TRPL spectra, which could be described with a double exponential decay

function, suggesting two decay processes, a non-radiative recombination process and a radiative recombination process. The charge carrier lifetimes are shown in Table S4. The average lifetime for the pure perovskite is 602.0 ns, but dropped to 30.1 ns for PVSK/PCBM sample, due to charge-carrier transfer from PVSK to PCBM, giving rise to the TRPL intensity quenching. The further decrease in the TRPL intensity and shorter lifetime of 14.5 ns for PVSK/Y6 suggests a faster charge transfer for the PVSK/Y6 than the PVSK/PCBM. This is also in agreement with the reduction in trap density of states (t-DOS) in the complete devices, as shown in Figure 3e. The t-DOS distribution can be obtained from the frequency dependent capacitance using $DOS\ (E_\omega) = -\frac{V_{bi}}{qW}\frac{d_c}{d_\omega}\frac{\omega}{KT}$, where V_{bi}, q ,W, C, ω, K, and T correspond to the following: the built-in potential, elementary charge, depletion width, capacitance, angular frequency, Boltzmann constant and temperature, respectively.[33] V_{bi} can be obtained from the $1/C^2$–V Mott-Schottky plots shown in Figure 3f, where V_{bi} is given by the intersection on the bias axis.[34] As shown in Figure 3e, the device with Y6 had a lower t-DOS over the entire trap depth region. The t-DOS with the shallow trap region of ~0.30-0.42 eV is assigned to traps at grain boundaries/interfaces, while the deeper region of 0.50-0.60 eV refers to the bulk defects inside the perovskite films.[33,35] It is well known that solution-processed perovskites often have defects,[36] such as impurities, vacancies and interstitials both in the bulk and at the surface, and dangling bonds at boundaries and surfaces, which, in addition to the energy disorder of ETLs, all of which can result in nonradiative recombination of photo-carriers, preventing the devices from hitting their theoretical efficiency limit.[22] The t-DOS results in this study show that the non-radiative recombination in Y6 device is significantly reduced, which is consistent with the enhanced V_{oc} and FF.

We used x-ray photoelectron spectroscopy (XPS)[37] and the total fluorescence yield (TFY) spectra [38] near the N-edge to explore possible molecular bonding/chemical interactions between

the perovskite and Y6, which are possible origins of decreased t-DOS and operational device stability with external stress. Figure 4a-d and Figure S9 show the XPS spectra of characteristic C-F, C=O, C-S-C, C≡N groups and Pb 4f at the PVSK/Y6 interface. The control samples are pure Y6 and pure perovskite films on ITO substrates. As seen in Figure 4a, the F 1s peak shifted by ~ 0.2 eV to a higher energy and O 1s peak shifted by ~ 1.3 eV, originating from a higher oxidation state arising from the additional Coulombic interaction between the photoemitted electrons and the ion core. The additional interactions could result from new Pb-F and Pb-O binding.[39-42] New S 2p peaks of PbS appearing in Figure 4c confirmed the chemical interaction between Pb^{2+} in perovskite and C-S-C in Y6 directly. However, no obvious peak shifting of Pb 4f (Figure S9) was observed, which could be due to the large amount of Pb-I (perovskite) bindings on the surface of PVSK/Y6 film, and only small part of Pb defects or PbI_2 residue were passivated by Y6. There are three different C-N bindings in the perovskite (MA^+ ($C\text{-}NH_2^+$), FA^+($C{=}NH_2^+$, $C\text{-}NH_2$)), while there are 4 different C-N bindings in Y6 (C-N-C, C=N-S and two kinds of C=C≡N). No features can be distinguished from the XPS N 1s spectrum due to significant overlap of possible peaks. High-resolution synchrotron-based TFY measurements were performed to track the evolution of the $\pi^*_{C\equiv N}$ resonances in Y6. Figure 4d shows the TFY $\pi^*_{C\equiv N}$ transition peaks emerged at 398-400 eV. The near disappearance of the peak located at 398-399 eV in the PVSK/Y6 sample indicates an electron loss from C≡N in Y6, probably transfer to perovskite (Pb^{2+}). The molecular interactions were further simulated by density functional theory (DFT) calculations (Figure 4e and Figure S10).[43] The Y6 molecule initially lays down on the PVSK surface without specific connections. The geometry was then optimized by VASP. After optimization, C≡N was blended and connected with surface Pb atoms, which suggests that C≡N could be the most effective electron-donating group to passivate the Pb traps on the perovskite surface. This is further confirmed by a very recent

report on the passivation of a small molecular, 6TIC-4F, on the inorganic perovskite by comparing the formation of F-Pb, N-Pb and S-Pb where the N-Pb bonding motif has the largest formation energy.[44] Here, in our simulation, the binding energy ($E_{binding}=E_{combined}-E_{surface}-E_{molecule}$) of Y6 with perovskites is calculated to be -0.64 eV, which is much higher than that for $PC_{61}BM$ (-0.11 eV), indicating stronger interactions at PVSK/Y6 interfaces. We also performed simulations on the PVSK/ETL interface to compare the charge injection efficiency. The density of states and corresponding orbitals of a PCBM adsorbed on a perovskite surface are shown in Figure S10a. The conduction band lays about 0.4 eV below the Fermi level. The HOMO of PCBM is located near a defect level of adsorption. Due to the limited thickness layer, a lot of the surface states are presented in the range of [-0.4 eV, -0.1 eV], which are mixed with the conduction band edge. The LUMO and LUMO-1 of PCBM are ~0.2 eV lower than the conduction band. The electron injection driving force is 0.2 eV, which suggests that the electron injection could be very efficient. One should note that the existence of the large number of surface states is due to the thin slab model, which cannot represent the real surface of a bulk perovskite. Figure S10b gives the density of states of the model of a Y6 molecule adsorbed on a perovskite surface and the corresponding orbitals. The valence band of perovskite is about 0.2 eV below the Fermi level, The HOMO of Y6 molecule is slightly higher than the valence band. Since the layer is not thick enough, surface states are seen between 0.3 to 0.9 eV. The LUMO of Y6 molecules aligns at 1.0 eV. Hence, the gap of Y6 molecule is 1.1 eV in our calculation. The conduction band of the perovskite is 0.2 eV above LUMO, just as for PCBM, meaning they should show similar charge injection efficiencies. These molecule-scale chemical interactions studied by XPS, TFY, and DFT unveil the underlying reasons of the reduction in trap states (as shown in Figure 4f) at the PVSK/Y6 interface,

suppressing the non-radiative recombination and delivering the higher efficiencies and better stabilities.

Charge Carrier Dynamics at the Perovskite/Y6 Interface

In order to understand whether excitons generated in Y6 dissociate at the PVSK/Y6 interface akin to an organic photovoltaic (OPV) bulk-heterojunction (BHJ) system (like PM6:Y6 BHJ), we conducted steady-state microwave conductivity (SSMC)[45-46] and ultrafast transient absorption spectroscopy (TAS) measurements on neat films of Y6, PVSK and the PVSK/Y6 bilayer. We compared the results to those of a control OPV BHJ system (neat polymer donor PM6 and the BHJ with Y6). The SSMC measurement is essentially an IQE of equilibrium-state photoinduced charge generation, where the absolute signal is a product of the yield of carriers generated, weighted by their respective motilities, and their charge-separated lifetime (ϕ x $\Sigma\mu$ x τ), recorded here over a monochromated excitation range. A compliment to the EQE measurement, SSMC contactlessly probes the sample with GHz frequency microwaves, meaning that with both techniques we can compare the QE response of the PVSK/Y6 interface either with or without contacts to help understand the mechanism and origin of the observed NIR photocurrent (in Figure 1e). We investigated whether the PVSK/Y6 interface mimics the charge generation interface found in an OPV blend, where a donor-acceptor energy offset provides sufficient driving force to split the exciton. As shown in Figure 5a, the PM6:Y6 BHJ sample shows that long-lived free carriers are generated when Y6 is excited (PM6 does not absorb at wavelengths longer than 680 nm, Figure 5b) as evidenced by SSMC signal at wavelengths of 680 to 910 nm, perfectly tracking the absorption contributions of Y6. In contrast, the SSMC signal for the PVSK/Y6 samples only appears once the excitation wavelength meets the band edge of the perovskite. These results clearly

indicate that the mechanism responsible for NIR photocurrent at the PVSK/Y6 interface is not the same as in OPVs.

This notion is further supported on a different time-scale in the TAS data (Figure 5c-5f and Figure S11). There is a slightly faster decay of the PVSK bleach kinetics after its direct excitation in the PVSK/Y6 film compared with the neat PVSK film (Figure S11a), supporting the PL result of some charge-transfer across the interface with Y6 in Figure 3c. However, the TAS data show no bleach of the PVSK band edge after excitation of the Y6 component (Figure 5d), and the kinetics of the Y6 bleach in neat vs. PVSK/Y6 films is identical when it is directly excited at 890 nm (Figure S11b), meaning electron transfer into Y6 may be slightly more favorable than splitting Y6 excitons at the PVSK interface. In contrast, the PM6:Y6 BHJ show signatures of polaron bands at 780 nm (black arrow in Figure 5e and red arrow in Figure 5f) regardless of excitation of the PM6 or Y6 component. The mirror-image kinetics of polaron rise vs. bleach decay after photoexcitation of each component of the PM6:Y6 BHJ (Figure S11c-d) are a strong indicator of direct and efficient interfacial charge transfer. The fact that electron injection from PVSK to Y6 occurs when the PVSK is excited, but exciton splitting and hole injection from Y6 to PVSK is not observed when Y6 is excited is a thought-provoking result, especially considering that Y6 by itself produces as much photocurrent as when traditional BHJ is used.[47,48] As such, we do not know the exact mechanism responsible for photocurrent from the Y6 layer, but rather conclude from the SSMC and TAS data that charge generation at the PVSK/Y6 interface is not the same as at the PM6:Y6 BHJ interface. One explanation could be that the built-in potential of the device, where metal contacts are present, provides sufficient additional driving force to split the exciton, but certainly more studies are warranted to further understand the origin of, and

possibly improve, photocurrent due to absorption exclusively by the MFIL, which will also provide guidance on the PVSK/BHJ research.

Device Stability and Ion Migration Suppression

Stability is currently the biggest challenge for PSCs in practical application. Among the severe work environment (heating, light, mechanical stress, etc), humidity has been shown to be a major stressor causing perovskite-based device degradation. Integrating a hydrophobic barrier layer has been shown to decrease moisture corrosion. However, previous reports have mostly focused on a post modification either on the perovskite surface[14] or charger transfer layer[49] to enhance the hydrophobicity, while a MFIL that works as a complementary light absorber, a charge carrier transport medium, as well as a hydrophobic moisture barrier has never been reported. The Y6-based device not only shows improved device efficiency, but also exhibits superior device stability after light and moisture exposure as well as thermal annealing. The water contact angle (shown in Figure 6a) for the PVSK/PCBM film is 74.0°, while that for the PVSK/Y6 film was 86.7°. The increased contact angle suggests an increased hydrophobicity. This was also confirmed by depositing water droplets directly on the PVSK/ETL films for 5 min, simulating a rainfall atmosphere, as shown in Figure 6a. The PVSK/PCBM film began to degrade immediately and became totally yellow in 1 min, implying that the water quickly penetrates into the perovskite through PCBM. In contrast, the PVSK/Y6 showed a much higher water tolerance, and only minor spots emerged at the film edges while most of the perovskite covered with Y6 still retained black.

To demonstrate the stability of devices with different ETLs under operational conditions, non-encapsulated solar cells were aged under AM 1.5G 100 $mW \cdot cm^{-2}$ solar irradiation, ambient stability with humidity of 60%-65% (Figure 6d). The Y6-based devices maintained over 95% of their initial efficiencies (T95 lifetime) after 1300 min of accelerated aging in ambient environment,

whereas the devices with the PCBM layer degraded to 95% in 60 mins, and to 90% within 150 min. The T95 lifetime of Y6 device is 20 times longer than the PCBM-based device. In addition, the Y6 device showed substantial long-term stability upon moisture (humidity of 60%-65%), and retained 72% of its initial PCE after 1700 hrs (~70 days) without encapsulation, while the PCBM devices almost fully degraded (Figure 6e). The long-term stability of characteristic photovoltaic performance parameters is shown in Figure S12, and all the parameters retained ~90% of the initial value, especially for the J_{sc}, which only suffered 5% loss in two months. Furthermore, The Y6 device also showed superior thermal stability. Upon aging at 85 °C in N_2 atmosphere, 95% of the initial efficiency was retained after 1000 hrs (Figure 6f and Figure S13), while the PCBM devices decreased to 75% of output after 1000 hrs of continuous thermal annealing. These results demonstrate superior moisture, light and thermal stability of Y6-based devices in comparison to the PCBM device. These are among the best stability results reported for PSCs with inverted structures.

Time-of-flight secondary ion mass spectrometry (ToF-SIMS) was used to probe the ion distribution as a function of depth. ToF-SIMS profiles of selected different elements are shown in Figure 6b and 6c. Strikingly, a I^- peak signal is seen in the PCBM/Ag interface (Figure 6b), whereas no I^- accumulation is found in the Y6/Ag interface (Figure 6c), confirming the I^- migration into the PCBM during operational aging (MPP tracking with light illumination and humidity of 60%-65%). The I^- migration is a recognized phenomenon in lead halide perovskites due to the low activation energies required for formation and/or transport of the ion migration.[50] As there are high density of ionic defects in polycrystalline perovskites, the migration and accumulation of I^- become more severe under operational conditions. These results in Figure 6b is also consistent with previous reports, and the ion diffusion from the perovskite to the silver electrode was directly

observed by ToF-SIMS with different aging protocols, and the generation of an AgI barrier accelerated the device degradation.[51] In addition to the I^- migration, there is obvious O^- signal in the Ag layer and an enhanced O^- intensity in PCBM layer (Figure S14), reflecting the oxidation of Ag electrode and possible moisture invasion throughout the devices. These results unveil that the Y6 layer can efficiently reduce the trap states in perovskite, and suppress I^- migration and moisture infiltration, preventing the perovskite degradation and boosting the long-term device stability.

Conclusion

In summary, we have demonstrated a new strategy to utilize multifunctional interface layer to simultaneously enhance the device efficiency and operational stability in p-i-n perovskite solar cells. A series of narrow-band gap NFAs was studied to further explore the criterions for screening the MFIL materials. A molecular narrow-bandgap organic semiconductor, Y6, was selected as a MFIL here, to instead of the traditional PCBM ETL in inverted PSCs, provides extended light absorption, moisture barrier, and enhanced electron collection, leading to an increased PCE of 21.0% and enhanced operational stability upon light, heating and moisture as long as ~1700 hrs. We showed that the solvents for processing Y6 molecules have significant impact on the molecular orientation and crystallization of Y6. Compare to Y6-CB and Y6-Tol, the Y6-CF with unique 2D packing and π-π stacking predominating the charge carrier extraction and transport, achieved the highest photocurrent enhancement and champion device efficiency. Meanwhile, the charge carrier dynamics at NIR was preliminary explored by SSMC and TAS, and the built-in potential of the device was proposed to provide sufficient additional driving force to split the excitons produced in Y6. The reduced trap density states contributed to the decreased non-radiative recombination and faster charge transfer in Y6-based devices in comparison to PCBM-based devices, leading to the increased PCE from ~ 19% to ~ 21%. Detailed molecular bindings at the critical PVSK/Y6

interface were further analyzed by XPS and TFY measurements, which could explain the reduced trap states and suppressed ion migration and moisture infiltration, evidenced by Tof-SIMS measurements. Correlations between molecular orientation, interface molecular bonding, trap state density, non-radiation recombination, and device performance were established. These results present new insights for the design of novel interface layers, open a new window to simplify the device structure with MFIL in PSCs, and will also significantly impact the use of perovskite-based optoelectronics for future applications.

References

1. Li, Z., Klein, T.R., Kim, D.H., Yang, M., Berry, J.J., van Hest, M.F.A.M., and Zhu, K. (2018). Scalable fabrication of perovskite solar cells. Nat. Rev. Mater. *3*, 18017.
2. Lee, C.C., Chen, C.I., Liao, Y.T., Wu, K.C., and Chueh, C.C. (2019). Enhancing efficiency and stability of photovoltaic cells by using perovskite/Zr-MOF heterojunction including bilayer and hybrid structures. Adv. Sci. *6*, 1801715.
3. Zheng, Y., Su, R., Xu, Z., Luo, D., Dong, H., Jiao, B., Wu, Z., Gong, Q., and Zhu, R. (2019). Perovskite solar cell towards lower toxicity: A theoretical study of physical lead reduction strategy. Sci. Bull. *64*, 1255-1261.
4. Best research-cell efficiency chart, NREL, https://www.nrel.gov/pv/cell-efficiency.html.
5. Jena, A.K., Kulkarni, A., and Miyasaka, T. (2019). Halide perovskite photovoltaics: background, status, and future prospects. Chem. Rev. *119*, 3036-3103.
6. Hu, Q., Zhao, L., Wu, J., Gao, K., Luo, D., Jiang, Y., Zhang, Z., Zhu, C., Schaible, E., Hexemer, A.*, et al.* (2017). In situ dynamic observations of perovskite crystallisation and microstructure evolution intermediated from $[PbI6]^{4-}$ cage nanoparticles. Nat. Commun. *8*, 15688.
7. Wang, K., Subhani, W.S., Wang, Y., Zuo, X., Wang, H., Duan, L., and Liu, S. (2019). Metal cations in efficient perovskite solar cells: progress and perspective. Adv. Mater. *31*, 1902037.
8. Deng, W., Liang, X., Kubiak, P.S., and Cameron, P.J. (2018). Molecular interlayers in hybrid perovskite solar cells. Adv. Energy. Mater. *8*, 1701544.
9. Wang, L., Zhou, H., Hu, J., Huang, B., Sun, M., Dong, B., Zheng, G., Huang, Y., Chen, Y., Li, L.*, et al.* (2019). A Eu^{3+}-Eu^{2+} ion redox shuttle imparts operational durability to Pb-I perovskite solar cells. Science *363*, 265.
10. Tu, Y., Xu, G., Yang, X., Zhang, Y., Li, Z., Su, R., Luo, D., Yang, W., Miao, Y., Cai, R.*, et al.* (2019). Mixed-cation perovskite solar cells in space. Science China Physics, Mechanics & Astronomy *62*, 974221.
11. Meng, L., You, J., and Yang, Y. (2018). Addressing the stability issue of perovskite solar cells for commercial applications. Nat. Commun. *9*, 5265-5265.
12. Bai, S., Da, P., Li, C., Wang, Z., Yuan, Z., Fu, F., Kawecki, M., Liu, X., Sakai, N., Wang, J.T.-W.*, et al.* (2019). Planar perovskite solar cells with long-term stability using ionic liquid additives. Nature *571*, 245-250.
13. Jung, E.H., Jeon, N.J., Park, E.Y., Moon, C.S., Shin, T.J., Yang, T.-Y., Noh, J.H., and Seo, J. (2019). Efficient, stable and scalable perovskite solar cells using poly(3-hexylthiophene). Nature *567*, 511-515.
14. Yang, S., Chen, S., Mosconi, E., Fang, Y., Xiao, X., Wang, C., Zhou, Y., Yu, Z., Zhao, J., Gao, Y.*, et al.* (2019). Stabilizing halide perovskite surfaces for solar cell operation with wide-bandgap lead oxysalts. Science *365*, 473.
15. Luo, D., Yang, W., Wang, Z., Sadhanala, A., Hu, Q., Su, R., Shivanna, R., Trindade, G.F., Watts, J.F., Xu, Z.*, et al.* (2018). Enhanced photovoltage for inverted planar heterojunction perovskite solar cells. Science *360*, 1442.
16. Liu, T., Chen, K., Hu, Q., Zhu, R., and Gong, Q. (2016). Inverted perovskite solar cells: progresses and perspectives. Adv. Energy. Mater. *6*, 1600457.
17. Chen, H., Wei, Q., Saidaminov, M.I., Wang, F., Johnston, A., Hou, Y., Peng, Z., Xu, K., Zhou, W., Liu, Z.*, et al.* (2019). Efficient and stable inverted perovskite solar cells oncorporating secondary amines. Adv. Mater. *31*, 1903559.

18. Tong, J., Song, Z., Kim, D.H., Chen, X., Chen, C., Palmstrom, A.F., Ndione, P.F., Reese, M.O., Dunfield, S.P., Reid, O.G., *et al.* (2019). Carrier lifetimes of >1 μs in Sn-Pb perovskites enable efficient all-perovskite tandem solar cells. Science *364*, 475.
19. Jošt, M., Köhnen, E., Morales-Vilches, A.B., Lipovšek, B., Jäger, K., Macco, B., Al-Ashouri, A., Krč, J., Korte, L., Rech, B., *et al.* (2018). Textured interfaces in monolithic perovskite/silicon tandem solar cells: advanced light management for improved efficiency and energy yield. Energy Environ. Sci. *11*, 3511-3523.
20. Yang, D., Yang, R., Priya, S., and Liu, S. (2019). Recent advances in flexible perovskite solar cells: fabrication and applications. Angew. Chem. *58*, 4466-4483.
21. Chen, W., Sun, H., Hu, Q., Djurišić, A.B., Russell, T.P., Guo, X., and He, Z. (2019). High short-circuit current density via integrating the perovskite and ternary organic bulk heterojunction. ACS Energy Lett. *4*, 2535-2536.
22. Luo, D., Su, R., Zhang, W., Gong, Q., and Zhu, R. (2019). Minimizing non-radiative recombination losses in perovskite solar cells. Nat. Rev. Mater. *5*, 44-60.
23. Akbulatov, A.F., Frolova, L.A., Griffin, M.P., Gearba, I.R., Dolocan, A., Vanden Bout, D.A., Tsarev, S., Katz, E.A., Shestakov, A.F., Stevenson, K.J., *et al.* (2017). Effect of electron-transport material on light-induced degradation of inverted planar junction perovskite solar cells. Adv. Energy Mater. *7*, 1700476.
24. Yuan, J., Zhang, Y., Zhou, L., Zhang, G., Yip, H.-L., Lau, T.-K., Lu, X., Zhu, C., Peng, H., Johnson, P.A., *et al.* (2019). Single-junction organic solar cell with over 15% efficiency using fused-ring acceptor with electron-deficient core. Joule *3*, 1140-1151.
25. Yao, H., Cui, Y., Yu, R., Gao, B., Zhang, H., and Hou, J. (2017). Design, synthesis, and photovoltaic characterization of a small molecular acceptor with an ultra-narrow band gap. Angew. Chem. *56*, 3045-3049.
26. Yan, C., Liu, T., Chen, Y., Ma, R., Tang, H., Li, G., Li, T., Xiao, Y., Yang, T., Lu, X., *et al.* (2020). ITC-2Cl: A versatile middle-bandgap nonfullerene acceptor for high-efficiency panchromatic ternary organic solar cells. Solar RRL *4*, 1900377.
27. Chen, Y., Liu, T., Hu, H., Ma, T., Lai, J.Y.L., Zhang, J., Ade, H., and Yan, H. (2018). Modulation of end groups for low-bandgap nonfullerene acceptors enabling high-performance organic solar cells. Adv. Energy. Mater. *8*, 1801203.
28. Liu, T., Luo, Z., Chen, Y., Yang, T., Xiao, Y., Zhang, G., Ma, R., Lu, X., Zhan, C., Zhang, M., et al. (2019). A nonfullerene acceptor with a 1000 nm absorption edge enables ternary organic solar cells with improved optical and morphological properties and efficiencies over 15%. Energy Environ. Sci. 12, 2529-2536.
29. Lilliu, S., Agostinelli, T., Pires, E., Hampton, M., Nelson, J., and Macdonald, J.E. (2011). Dynamics of crystallization and disorder during annealing of P3HT/PCBM bulk heterojunctions. Macromolecules *44*, 2725-2734.
30. Zhu, L., Zhang, M., Zhou, G., Hao, T., Xu, J., Wang, J., Qiu, C., Prine, N., Ali, J., Feng, W., *et al.* (2020). Efficient organic solar cell with 16.88% efficiency enabled by refined acceptor crystallization and morphology with improved charge transfer and transport properties. Adv. Energy Mater.1904234. https://doi.org/10.1002/aenm.201904234
31. Strawhecker, K.E., Kumar, S.K., Douglas, J.F., and Karim, A. (2001). The critical role of solvent evaporation on the roughness of spin-cast polymer films. Macromolecules *34*, 4669-4672.
32. Golubev, T., Liu, D., Lunt, R., and Duxbury, P. (2019). Understanding the impact of C60 at the interface of perovskite solar cells via drift-diffusion modeling. AIP Adv. *9*, 035026.

33. Zheng, X., Chen, B., Dai, J., Fang, Y., Bai, Y., Lin, Y., Wei, H., Zeng, Xiao C., and Huang, J. (2017). Defect passivation in hybrid perovskite solar cells using quaternary ammonium halide anions and cations. Nat. Energy. *2*, 17102.
34. Landi, G., Neitzert, H.C., Barone, C., Mauro, C., Lang, F., Albrecht, S., Rech, B., and Pagano, S. (2017). Correlation between electronic defect states distribution and device performance of perovskite solar cells. Adv. Sci. *4*, 1700183-1700183.
35. Walter, T., Herberholz, R., Müller, C., and Schock, H.W. (1996). Determination of defect distributions from admittance measurements and application to Cu(In,Ga)Se2 based heterojunctions. J. Appl. Phys. *80*, 4411-4420.
36. Aydin, E., De Bastiani, M., and De Wolf, S. (2019). Defect and contact passivation for perovskite solar cells. Adv. Mater. *31*, 1900428.
37. Chun-Ren Ke, J., Walton, A.S., Lewis, D.J., Tedstone, A., O'Brien, P., Thomas, A.G., and Flavell, W.R. (2017). In situ investigation of degradation at organometal halide perovskite surfaces by X-ray photoelectron spectroscopy at realistic water vapour pressure. Chem. Commun. *53*, 5231-5234.
38. Lin, F.; Liu, Y. J.; Yu, X. Q.; Cheng, L.; Singer, A.; Shpyrko, O. G.; Xing, H. L. L.; Tamura, N.; Tian, C. X.; Weng, T. C.; Yang, X. Q.; Meng, Y. S.; Nordlund, D.; Yang, W. L.; Doeff, M. M. Synchrotron X-ray Analytical Techniques for Studying Materials Electrochemistry in Rechargeable Batteries. Chem. Rev. 2017, 117, 13123-13186.
39. NIST X-ray Photoelectron Spectroscopy Database, Version 4.1, (2012), http://srdata.nist.gov/xps/.
40. Rondon, S., and Sherwood, P.M.A. (1998). Core level and valence band spectra of PbO by XPS. Surf. Sci. Spectra. *5*, 97-103.
41. Foreman, K., Echeverria, E., Koten, M.A., Lindsay, R.M., Hong, N., Shield, J., and Adenwalla, S. (2016). The metal/organic interface in cobalt/vinylidene fluoride heterostructures. Mater. Res. Express. *3*, 116403.
42. Lin, Y., Shen, L., Dai, J., Deng, Y., Wu, Y., Bai, Y., Zheng, X., Wang, J., Fang, Y., Wei, H., et al. (2017). π-conjugated lewis base: Efficient trap-passivation and charge-extraction for hybrid perovskite solar cells. Adv. Mater. 29, 1604545.
43. Butler, K.T., Sai Gautam, G., and Canepa, P. (2019). Designing interfaces in energy materials applications with first-principles calculations. Npj. Comput. Mater. *5*, 19.
44. Wang, J., Zhang, J., Zhou, Y., Liu, H., Xue, Q., Li, X., Chueh, C.-C., Yip, H.-L., Zhu, Z., and Jen, A.K.Y. (2020). Highly efficient all-inorganic perovskite solar cells with suppressed non-radiative recombination by a lewis base. Nat. Commun. *11*, 177.
45. Blackburn, J.L., Zhang, H., Myers, A.R., Dunklin, J.R., Coffey, D.C., Hirsch, R.N., Vigil-Fowler, D., Yun, S.J., Cho, B.W., Lee, Y.H*., et al.* (2020). Measuring photoexcited free charge carriers in mono- to few-layer transition-metal dichalcogenides with steady-state microwave conductivity. J. Phys. Chem. Lett. *11*, 99-107.
46. Labram, J.G., Perry, E.E., Venkatesan, N.R., and Chabinyc, M.L. (2018). Steady-state microwave conductivity reveals mobility-lifetime product in methylammonium lead iodide. Appl. Phys. Lett. *113*, 153902.
47. Guo, Q., Bai, Y., Lang, K., Yu, Z.-Z., Hayat, T., Alsaedi, A., Zhou, E., and Tan, Z.A. (2019). Expanding the light harvesting of $CsPbI_2Br$ to near infrared by integrating with organic bulk heterojunction for efficient and stable solar cells. ACS Appl. Mater. Inter. *11*, 37991-37998.
48. Daboczi, M., Kim, J., Lee, J., Kang, H., Hamilton, I., Lin, C.-T., Dimitrov, S.D., McLachlan, M.A., Lee, K., Durrant, J.R., et al. (2020). Towards efficient integrated perovskite/organic bulk heterojunction solar cells: Interfacial energetic requirement to reduce charge carrier recombination losses. Adv. Funct. Mater. 2001482.

49. Wu, C., Wang, K., Feng, X., Jiang, Y., Yang, D., Hou, Y., Yan, Y., Sanghadasa, M., and Priya, S. (2019). Ultrahigh durability perovskite solar cells. Nano. Lett. *19*, 1251-1259.
50. Lee, J.-W., Kim, S.-G., Yang, J.-M., Yang, Y., and Park, N.-G. (2019). Verification and mitigation of ion migration in perovskite solar cells. APL Materials *7*, 041111.
51. Li, J., Dong, Q., Li, N., and Wang, L. (2017). Direct evidence of ion diffusion for the silver-electrode-induced thermal degradation of inverted perovskite solar cells. Adv. Energy Mater. *7*, 1602922.

Acknowledgements

Dr. Q. Hu, Dr. W. Chen and W. Yang contributed equally to this work. Dr. Q. Hu and Prof. T. P. Russell were supported by the US Office of Naval Research under contract N00014-17-1-2241. This work was also financially supported by the National Natural Science Foundation of China (61775091, 51573076, 61722501 and 61805138). Dr. W. Chen and Prof. A. B. Djurišić are grateful for support from the Seed Funding for Strategic Interdisciplinary Research Scheme of the University of Hong Kong and RGC CRF grant 5037/18G. The authors thank Dr. Tao Liu and Prof. He Yan for the material of IOIC-2Cl and IEICO-4F, Dr. Xinle Li and Dr. Chongqing Yang for the discussion of XPS results, Prof. Benzhong Tang, Prof. Lu-tao Weng and Zaiyu Wang for the ToF-SIMS analysis, thank Dr. Wanli Yang for the discussions of TFY studies. TFY and GIXD were performed at beamline 11.0.1.2 and 7.3.3 at Advanced Light Source, Lawrence Berkeley National Laboratory, which was supported by the DOE, Office of Science, and Office of Basic Energy Sciences. We thank the support for sample preparation and device fabrication at Molecular Foundry, LBNL. Work at Molecular Foundry was supported by the Office of Science, Office of Basic Energy Sciences, the US Department of Energy under Contract No. DE-AC02-05CH11231. This work was supported in part by the National Renewable Energy Laboratory, operated by Alliance for Sustainable Energy, LLC, for the U.S. Department of Energy (DOE) through the Office of Basic Energy Sciences, Division of Chemical Sciences, Biosciences, and Geosciences under Contract No. DE-AC36-08GO28308.

Author Contribution

Q. H., T. P. R. and F. L. conceived the idea. T. P. R., F. L., and Z. H. supervised the project. Q. H., W. C. and W.Y. fabricated and optimized the perovskite solar cells, as well as the related device characterizations including the UV-vis absorption, PL/TRPL, t-DOS, EQE, STEM/SEM and so on. Q. H. and Y. L. performed GIWAXS. W. Z., Q. H. and C. W. conducted TFY measurements. Y. Z and J. X. performed the theoretical calculation. Y.-H. L. and M. S. conducted the KPFM measurements. Q. H. and L. K. conducted the XPS experiment. B.W. L., J. C. J. and Q. H. performed the SSMC and TAS measurements. Q. H. wrote the first draft of the paper, W. C., W. Y, Y. L., Y. Z., B.W. L. and J. C. J. revised the paper. All the authors discussed the results, and edited the manuscript.

Declaration of Interests

The authors declare no competing interest.

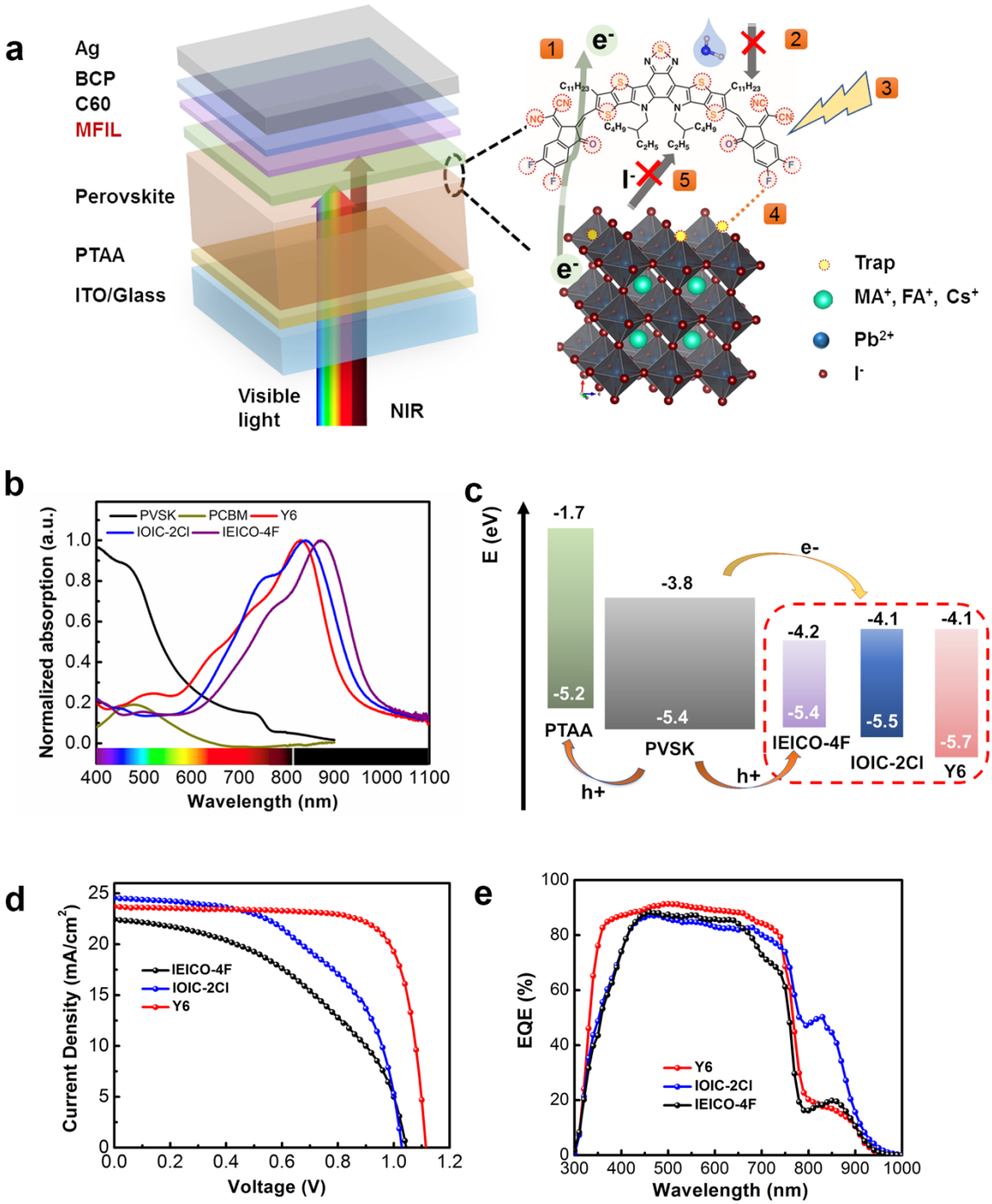

Figure 1. a) Schematic diagram of an inverted planar heterojunction perovskite solar cell based on the multi-functional interface layer (MFIL), and the functions marked in the diagram are 1) electron transporting, 2) moisture barrier, 3) near-infrared photocurrent enhancement, 4) trap passivation and 5) ion migration suppression. b) Normalized UV-vis absorption spectra of perovskite, and different electron transport layers. c) The energy level schema of the perovskite and the charge transport layers in this work. d) The *J-V* curves of PSCs based on three different narrow bandgap NFAs and e) the corresponding EQE spectra.

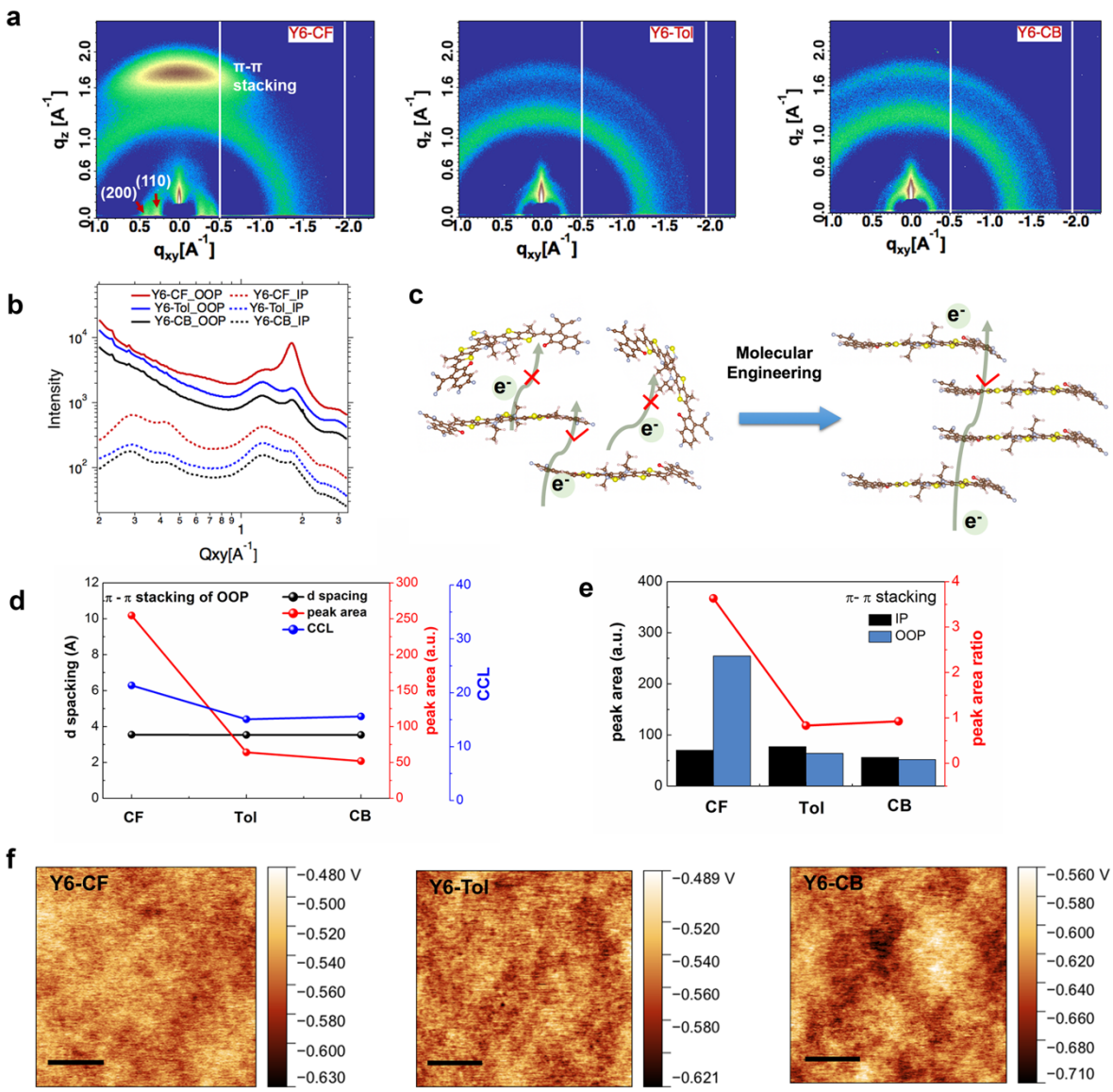

Figure 2. a) The 2D GIXD files and b) corresponding intergeated line-files for PVSK/Y6 films processed with different solvents. c) Molecular engineering and charge transfer in Y6 films with/without orientation. d)The d-spacing, peak area and the crystalline coherence length (CCL) of π-π stacking diffraction in out of plane direction. e) The peak ratio of π-π stacking diffraction in out of plane to the diffraction at in plane. (f) The surface potential distribution of perovskite/Y6 films measured by KPFM (the scale bars are 500 nm).

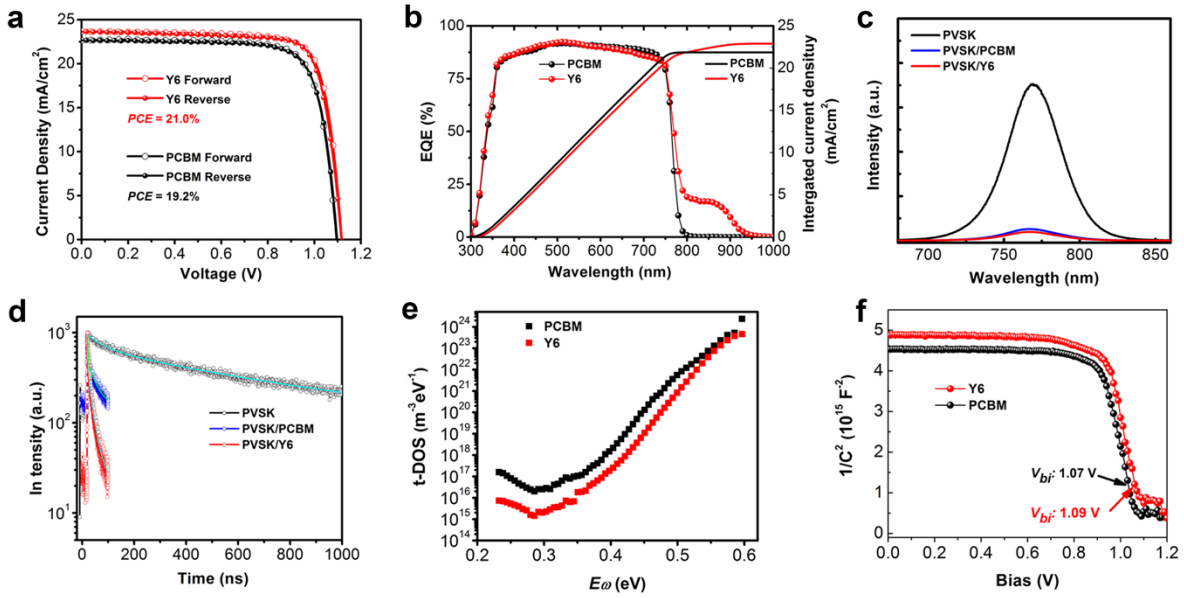

Figure 3. a) The *J-V* curves of PSCs based with Y6 and PCBM, separately. b) The corresponding EQE spectra. c) Steady-state and d) transient-time photoluminescence spectra. e) The t-DOS characteristics and f) Mott–Schottky characteristic results.

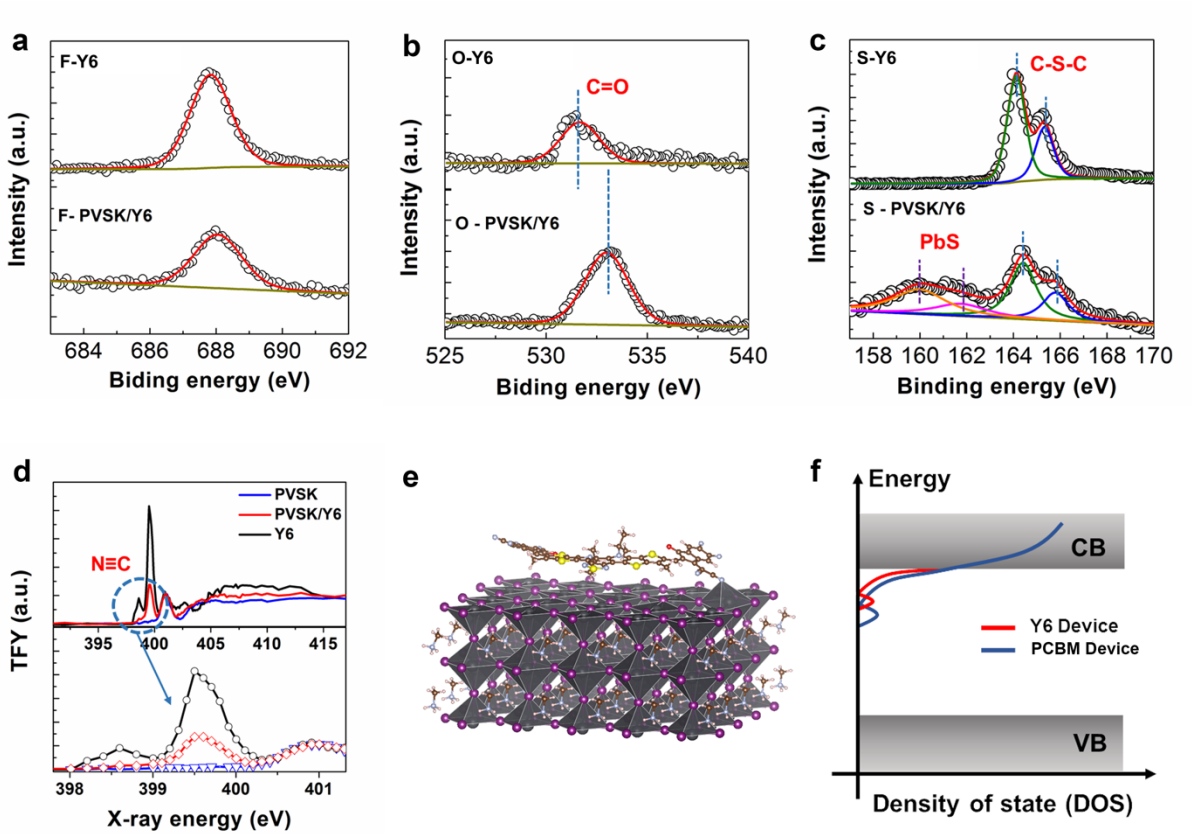

Figure 4. a-c) XPS spectra and d) TFY results of PVSK/Y6 interfaces. e) The schema of the molecular bonding between Y6 and perovskites. f) The diagram of the reduced trap states for Y6 based device compared to PCBM device.

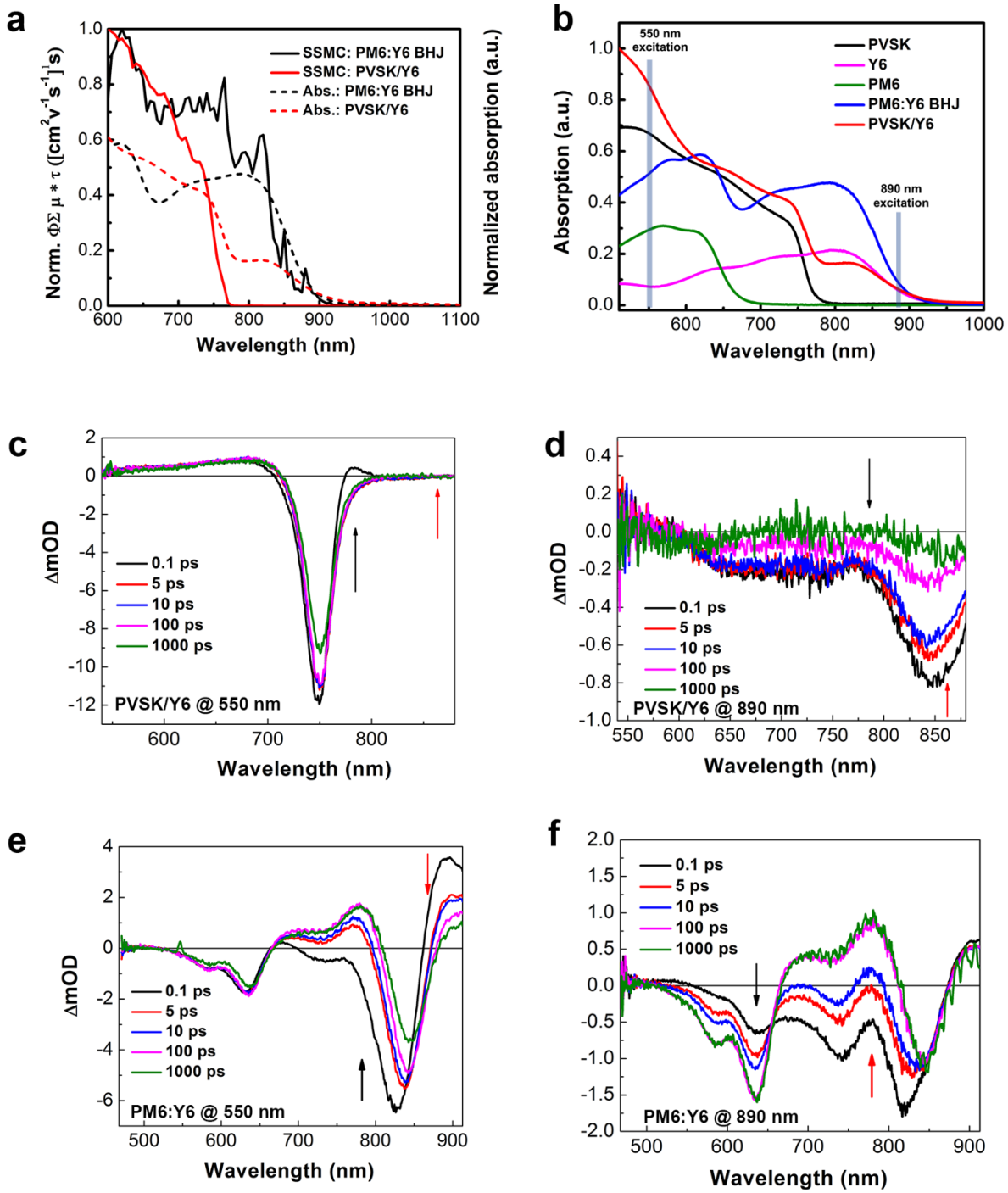

Figure 5. a) Steady-state microwave conductivity spectra and UV-vis absorption spectra of PM6:Y6 BHJ film and PVSK/Y6 film deposited on quartz substrates. b) UV-vis absorption spectra of the samples for TA measurements. c) Photoinduced absorption spectra collected at delay times shown in the legend for the PVSK/Y6 sample photoexcited at 550 nm (2.5 nJ pulse energy) and d) 890 nm (10 nJ pulse energy). Red and black arrows indicate positions chosen to monitor Y6 bleach and polaron absorption, respectively. e) Photoinduced absorption spectra collected at delay times shown in the legend for the PM6:Y6 BHJ sample photoexcited at 550 nm (2.5 nJ pulse energy) and f) 890 nm (10 nJ pulse energy). Red and black arrows indicate positions chosen to monitor PM6 bleach and polaron absorption, respectively.

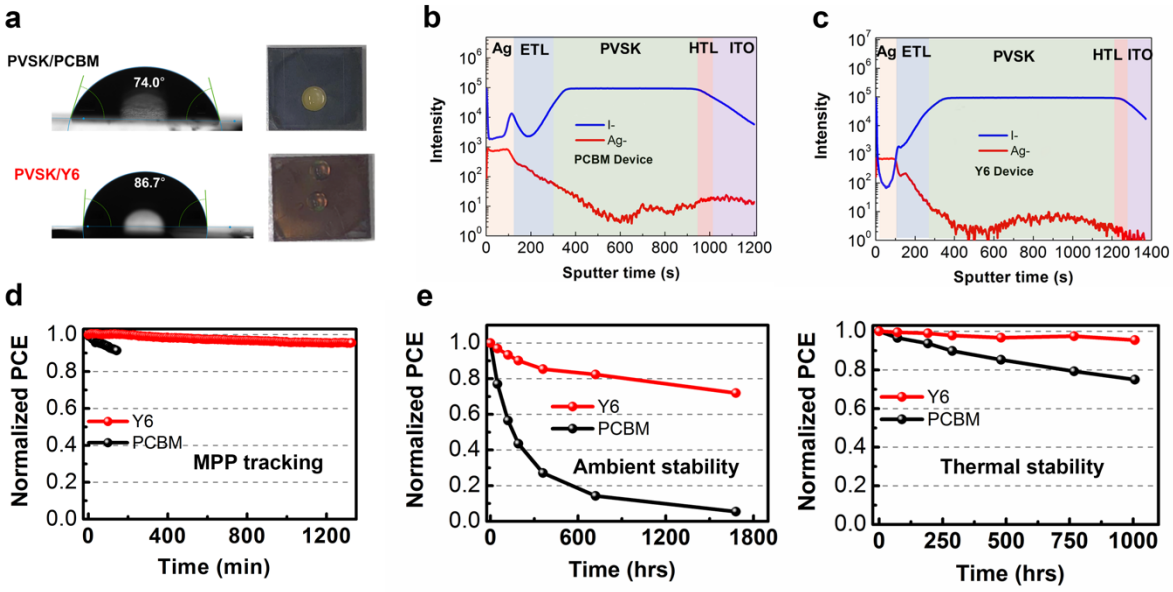

Figure 6. a) The water contact angle of perovskite/ETLs films (left) and the corresponding photoimages of water testing results (right). b) ToF-SIMS results of the aged PCBM based and c) Y6 based whole devices. d) The maximum power point tracking (MPPT) of perovkite devices under AM 1.5G 1sun illumination in ambient air with a relativity humidity of 60%~65% for ~1400 mins. e) The device ambient stability test upon a relativity humidity of 60%~65% at room temperature under dark for ~1700 hrs. f) The device thermal stabity test upon 85 °C in inert enviroment (glove box) under dark for 1000 hrs.